Performance of the 1-MJ, Wetted-Foam Target Design for the National Ignition Facility

Introduction

The primary mission of the National Ignition Facility (NIF)[1] is to demonstrate fusion ignition via inertial confinement fusion (ICF).[2] In the direct-drive[3,4] approach to ICF, a spherical target is illuminated by a number of laser beams arranged symmetrically in a configuration that provides adequate drive symmetry. The target shell is accelerated inward as its outer layers expand due to ablation. After the end of the laser pulse, shock dynamics and compression of the contained gas cause the shell to decelerate. During both the acceleration and deceleration phases of the implosion, the target is subject to Rayleigh–Taylor (RT) instability (see Ref. 3 and references therein)—first on the outer, then the inner surface of the shell. The acceleration-phase instability is seeded by the roughness of the outer surface of the shell, by nonuniformities in the illumination profiles of the individual beams, by beam mispointing, by energy imbalance and mistiming between the various beams, by the drive nonuniformity inherent in the geometric arrangement of the beams, and by the feedout of perturbations to the ablation surface from the inner surface of the shell by means of rarefaction waves. The deceleration-phase RT instability is seeded by the initial roughness of the inner surface of the shell and by nonuniformities that feed through to the inner surface by laser-driven shocks. Target-fabrication techniques have been developed to improve the target-surface smoothness, including the use of β-layering of the DT-ice surface.[5] The single-beam nonuniformities may be reduced through various beam-smoothing methods, such as smoothing by spectral dispersion (SSD),[6] polarization smoothing,[7] or distributed phase plates.[8] Even with these techniques, a target must be designed in such a way as to remain integral during the implosion and uniform enough to produce a hot spot that can initiate a burn wave in the fuel of the shell.

In this article, we present a target design that uses a plastic foam ablator saturated with deuterium–tritium (DT) ice (so-called "wetted foam"). Due to the dependence of inverse bremsstrahlung absorption on the atomic number ($\kappa \sim \langle Z^2 \rangle / \langle Z \rangle$ see Ref. 9), the wetted foam has a higher laser-coupling efficiency than pure DT. Plastic foam shells were originally proposed as a matrix for liquid DT fuel.[10] Others[11,12] proposed the use of foam as an ablator, in conjunction with a high-atomic-number material. In these designs, radiation from the high-atomic-number material preheats the foam, increasing the ablation velocity and reducing outer-surface instability. In the design presented here, the wetted foam is used primarily because of the increase in laser absorption.[13] Other proposed uses of foam include target designs for inertial fusion energy,[14] as well as for reduction of laser imprint.[15]

The stability of this design with respect to the primary sources of target and drive nonuniformity has been determined using two-dimensional (2-D) simulations with the hydrocode *DRACO*.[16] To weigh the effects of these different sources, a nonuniformity-budget analysis is performed in the manner of McKenty *et al.*[17] This analysis maps nonuniformity from different sources to a parameterization of the inner-shell-surface spectrum at the end of the acceleration phase, which in turn allows prediction of target performance. Following a description of the design in the next section, the tolerance of the design to nonuniformity sources is presented; the results from integrated simulations including ice and surface roughness, multiple-beam nonuniformity (primarily due to port geometry and power imbalance between beams), and imprint are shown; and, finally, the conclusions from the nonuniformity-budget analysis and the integrated simulations are presented.

The 1-MJ, Wetted-Foam Design

The 1.5-MJ, all-DT, direct-drive point design for symmetric drive on the NIF, shown in Fig. 109.25(a), consists of a DT shell surrounded by a thin layer of plastic (CH; see Ref. 17). The same design, scaled to an incident energy of 1 MJ, and the 1-MJ wetted-foam design are shown in Figs. 109.25(b) and 109.25(c). An incident energy of 1 MJ has been chosen to match energy restrictions to reduce the risk of damage to the NIF's optical elements. Table 109.III shows that the laser absorption, averaged over the length of the laser pulse, is ~60% to 65% for the all-DT designs. When part of the DT shell is replaced by a $CH(DT)_4$ wetted-foam ablator, the higher-average atomic number of the ablator results in an absorption of 86%

(Table 109.III). This allows a greater fraction of the incident laser energy to be converted to shell kinetic energy, allowing a thicker shell to be driven. The resulting 1-D gain for the 1-MJ, wetted-foam target is ~10% higher than that of the 1.5-MJ, all-DT design.

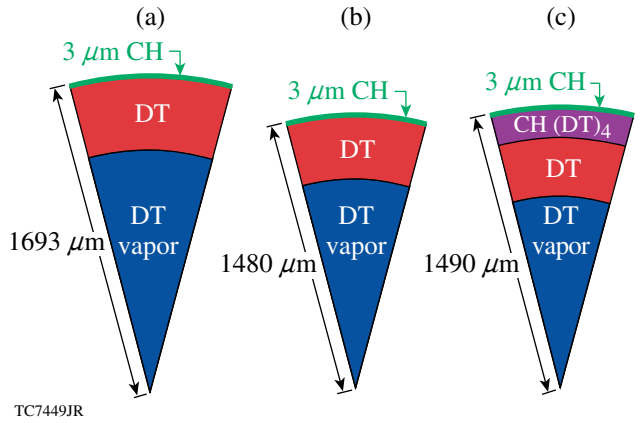

Figure 109.25
(a) The 1.5-MJ, all-DT, direct-drive target design for the NIF, (b) the same design scaled for an incident laser energy of 1 MJ, and (c) the 1-MJ, wetted-foam design. The wetted-foam shell is 326 μm thick, with 216 μm of pure DT fuel.

Table 109.III: Properties of the 1.5-MJ, all-DT; 1-MJ, all-DT; and 1-MJ, wetted-foam designs. Here A is the rms bubble amplitude at the end of the acceleration phase and ΔR is the in-flight shell thickness.

	All-DT	Scaled, All-DT	Wetted-foam
Energy (MJ)	1.5	1	1
Target radius (μm)	1695	1480	1490
Absorption (%)	65	59	86
$A/\Delta R$ (%)	30	33	11
Gain	45	40	49

The density of $CH(DT)_4$ is 304 mg cm^{-3}, corresponding to a dry-foam density of 120 mg cm^{-3}, given that during the freezing process the liquid DT contracts in volume by 17%, leaving voids in the wetted-foam layer. This is only 22% greater than the density of pure DT ice. This dry-foam density provides higher absorption, while not generating enough radiation to appreciably raise the fuel isentrope (as measured by the adiabat α, given by the ratio of the pressure to the cold Fermi-degenerate pressure). The wetted-foam-layer thickness ensures that the foam is entirely ablated by the end of the laser pulse. In an ignition design such as this, the first laser-driven shock, whether steady or, for picket designs, decaying, determines the shell adiabat. This is the only strong laser-driven shock, and it is the only shock to encounter unmixed foam and DT. High-resolution hydrodynamic simulations modeling the wetted-foam mixture have shown that after the initial undercompression behind the first shock,[18] the flow variables asymptote to within a few percent of the Rankine–Hugoniot values for ICF-relevant shock strengths.[19] These simulations demonstrate that the fluctuation decay scale length behind the shock is less than 2 μm, where this scale length is defined for a quantity q as $Lq = dr/d\ln\langle q\rangle$, and $\langle q\rangle$ is the average of q in the shock frame in the direction perpendicular to the shock [see Eq. (1) of Ref. 19]. These findings allow the wetted-foam layer to be modeled as a homogeneous mixture in the simulations described here.

Assuming an ICF shell remains intact during the acceleration phase, the most dangerous modes during deceleration are those that feed through from the outer to the inner surface. Modes feed through attenuated by a factor $\exp(-k\Delta R)$, where k is the wave number and ΔR is the shell thickness; the long-wavelength modes with $k \sim 1/\Delta R$ feed through most effectively. The number N of e-foldings of growth experienced by these modes during acceleration may be approximated by $N \sim \gamma\Delta t \sim (kgt^2)^{1/2}$, where γ is the growth rate over the time period Δt during which the shell is accelerated by the laser pulse, which is proportional to the classical growth rate for long-wavelength modes. Writing this in terms of the distance traveled by the shell, which is proportional to the initial outer shell radius R_0, $N \sim \left(R_0/\Delta R\right)^{1/2} \equiv (\mathrm{IFAR})^{1/2}$, where IFAR is the in-flight aspect ratio of the imploding shell. This is related to the implosion velocity v and the average shell adiabat by $\mathrm{IFAR} \sim v^2/\langle\alpha\rangle^{3/5}$ (Ref. 3). These relations show that the integrity of the shell during acceleration depends on the IFAR. The shell stability can be improved by lowering the implosion velocity or lowering the IFAR by increasing the shell thickness, which is equivalent to raising the average adiabat, since $\Delta R \sim \langle\alpha\rangle^{3/5}$. For a target where the adiabat is a constant function of shell mass, increasing the adiabat reduces the fuel compressibility and target gain. For a design such as this one, which has a shaped adiabat, N is reduced by a term proportional to $v\left(\alpha_{\mathrm{out}}/\langle\alpha\rangle\right)^{0.6}$, where α_{out} is the ablator adiabat.[20] The shell instability of the wetted-foam design is reduced from that of a 1-MJ-scaled, all-DT design by lowering the shell velocity by ~60 μm/ns (see Table 109.IV). As a result, the shell is less unstable during the acceleration phase, and the rms bubble amplitude divided by the shell thickness $A/\Delta R$, computed from 1-D simulations using a postprocessor,[21] is lower by a factor of 3 for the 1-MJ, wetted-foam design.

The increase in shell mass has the added benefit of raising the areal density of the shell at the time of ignition, making the shell more robust to deceleration-phase instabilities. Any RT growth on the inner edge of the shell during deceleration delays the onset of ignition, effectively lowering the shell velocity.[22] The inward motion of the shell at the time of ignition is necessary to offset the tremendous pressure the expanding burn wave exerts on the shell. If left unimpeded, the pressure of the burn wave would decompress the shell prematurely, quenching any possibility of high gain. In addition, decreasing the implosion velocity decreases the work done compressing the hot spot and reduces the hot-spot temperature. Further, a reduction in hot-spot temperature reduces the effects of ablative stabilization of the deceleration-phase RT instability. Due to these effects, the minimum energy needed for ignition scales with IFAR as $E_{ign} \sim (\text{IFAR})^{-3}$ (Ref. 20). The margin, defined as the inward-moving kinetic energy at ignition divided by the peak inward kinetic energy, is a measure of the additional kinetic energy of the shell above that needed for ignition. As seen in Table 109.IV, the decrease in IFAR and increase in shell mass have the effect of lowering the margin for the wetted-foam design. As will be shown in the following section, this design tolerates 1.75 μm of ice roughness, suggesting sufficient margin.

The laser pulse shape, shown in Fig. 109.26, uses an initial high-intensity picket to generate a decaying shock. As this shock propagates through the shell, its strength decreases to that supported by the foot, causing the level of shock heating to decrease from the ablator to the inner edge of the shell. This shapes the adiabat,[23] producing a high-ablator adiabat of ~10 while retaining a low-fuel adiabat of ~2. (Other adiabat-shaping techniques include the use of a relaxation picket where the

Table 109.IV: The wetted-foam design's shell is thicker than that of the all-DT design scaled to 1 MJ. This reduces shell instability and increases the areal density, but at the cost of a lower margin.

	V (μm/ns)	ΔR (μm)	IFAR	$A/\Delta R$ (%)	Areal density ρR (g/cm^2)	Margin (%)
1-MJ, all-DT	430	285	69	33	1.1	45
Wetted-foam	372	323	28	11	1.4	30

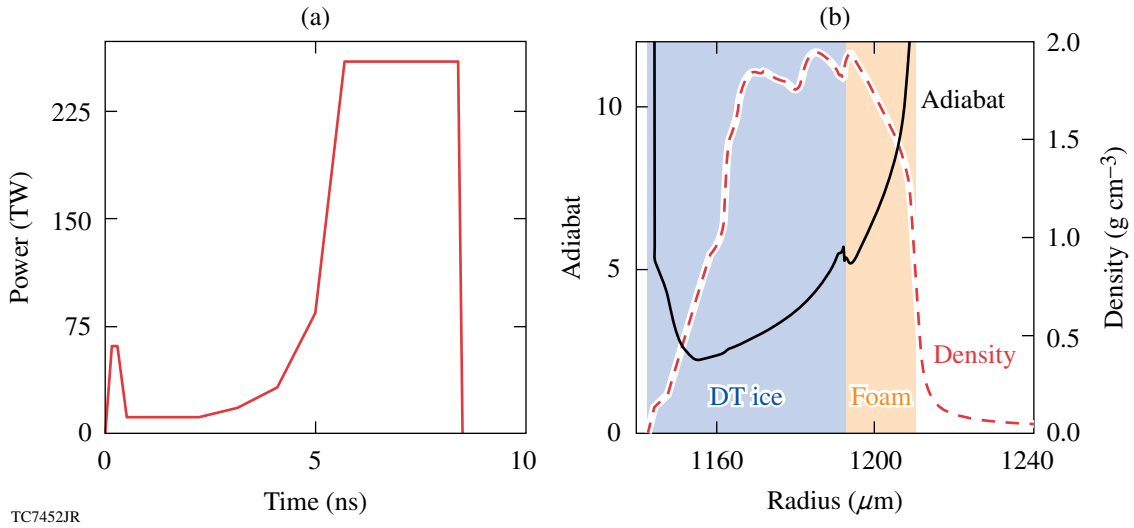

Figure 109.26
(a) The laser pulse and (b) the adiabat and mass density of the shell shortly after shock breakout. The laser pulse consists of an initial intensity spike or "picket" followed by a foot of low constant intensity and a rise to a high-power drive pulse.

laser intensity is zero between the picket and the foot pulse,[24] and a series of such isolated picket pulses preceding the main drive pulse.[12]) This technique reduces the shell instability and laser imprint during the acceleration phase since the ablation velocity is proportional to $\alpha^{3/5}$ (see Ref. 3). At the same time, it maintains the low-fuel adiabat needed to compress the fuel and achieve ignition. The picket also lowers imprint by decreasing the duration of the period of acceleration due to the outer CH layer and by increasing the rate of growth of the conduction zone between the ablation and critical surfaces.[25]

This design is robust to shock mistiming, critical for a successful ICF target design. The shock timing depends on accurate modeling of the equation of state (EOS) of the wetted-foam mixture and the DT. The effect on 1-D gain of changing either the foot length or power is shown in Fig. 109.27. These simulations show a reduction in gain of less than 10% for a variation in the foot-pulse length of ±250 ps, well within the NIF specification[26] of 100 ps. A change in power of ±4%, comparable to the NIF specification, produces a gain reduction of ~8%. It is anticipated that the shock timing will be verified experimentally using the materials of interest.

Nonuniformity-Budget Analysis

Four sources of nonuniformity contribute to the RT instability during the implosion. These include inner-surface DT-ice roughness, outer-surface roughness, and single-beam and multiple-beam nonuniformity. To gauge their relative importance and estimate their effects on target gain in an integrated simulation incorporating all four, a nonuniformity budget has been developed.[17,27] McKenty *et al.*[17] found that target gain may be approximated as a function of a weighted average of the inner-surface ice spectrum at the end of the acceleration phase,

$$\overline{\sigma} = \sqrt{a\sigma^2_{\ell<10} + \sigma^2_{\ell>9}},$$

regardless of the source of the ice perturbations. The low-mode weighting factor is $a = 0.06$. (The end of the acceleration phase is taken as the time when the ablation-front acceleration changes sign, shortly after the end of the laser pulse.) In 2-D simulations of the wetted-foam design incorporating various levels and spectral indices of ice roughness, it was found that this weighting factor provides reasonable scaling for this design as well.

This spectral weighting is based on the different effects that short-wavelength modes have on the hot spot. Any mode growth increases the hot-spot surface area, enhancing the cooling due to thermal conduction with the shell. For short wavelengths, the spikes of a single-mode perturbation on the inner surface of the shell lie close enough together that they cool below the temperatures at which they can contribute to α-particle generation. For these modes, the hot-spot size is effectively reduced by the physical extent of the perturbation.[28] Gain reduction becomes independent of wavelength for these high modes depending only on mode amplitude. Kishony and Shvarts[28] show that this behavior occurs for modes with $\ell > 9$. Because the dependence of yield on $\overline{\sigma}$ is independent of the source of the nonuniformity, the target gain may be estimated by adding the contributions to $\overline{\sigma}$ in quadrature and using the gain as a function of $\overline{\sigma}$ found, for instance, from simulations of just initial ice roughness.

Each of the sources of nonuniformity was simulated in 2-D. The laser-energy deposition was modeled using a straight-line ray-trace algorithm. To incorporate the reduction of coupling due to refraction, the absorbed energy determined from a 1-D simulation was used as the incident energy in 2-D simulations. This method provides a drive that closely replicates the adiabat

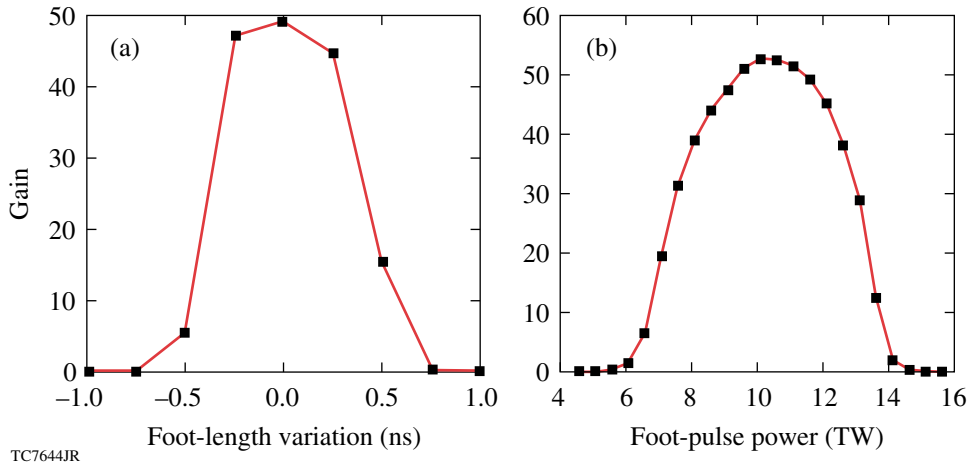

Figure 109.27
Sensitivity of the wetted-foam design's 1-D target gain to (a) deviation in the foot-pulse length and (b) foot-pulse power.

in the 1-D simulation. The pulse was truncated to ensure that the acceleration-phase stability, as determined using a 1-D postprocessor,[21] and the shell areal density at the time of ignition remained the same, and the implosion velocity differed by only 3%. Without refraction, however, the conduction zone is smaller, leading to more-efficient imprint.[29] It is expected that when these simulations are repeated using refractive laser-energy deposition, the target will be somewhat less sensitive to single-beam nonuniformity.

1. Initial DT-Ice Surface Roughness

The amplitude spectrum of initial inner-surface ice roughness has been found for cryogenic D_2 targets fabricated at LLE and is approximated here by a power law in mode number $A_\ell = A_0 \ell^{-\beta}$, where $\beta \sim 2$. The power for these modes lies primarily in $\ell < 50$. A series of 2-D simulations of ice-surface roughness were performed for various spectral amplitudes A_0 and power-law indices β, including modes 2 to 50. The resolution used for these simulations was about eight zones per wavelength for $\ell = 50$. The target gain as a function of initial rms ice roughness for $\beta = 2$ is shown in Fig. 109.28(a). This target was found to withstand 1.75 μm of initial ice roughness with little degradation in performance. When a power-law index of 1.5 was used, this design showed greater tolerance to ice roughness than the 1.5-MJ design presented in Ref. 17. This is most likely because of the higher areal density, 1.4 g cm^{-2}, of the wetted-foam design.

Figure 109.28(b) shows the shell at the time of ignition, when the hot-spot ion temperature has reached 10 keV. The density contours show that the hot spot is primarily distorted by modes 2 to 6. The dependence of gain on $\overline{\sigma}$ is shown in Fig. 109.29. It can be seen that this 1-MJ design can tolerate a $\overline{\sigma}$ of slightly less than 1 μm, compared with ~2 μm for the 1.5-MJ design of Ref. 17. For $\overline{\sigma} \gtrsim 0.8$ μm in the wetted-foam design, the RT

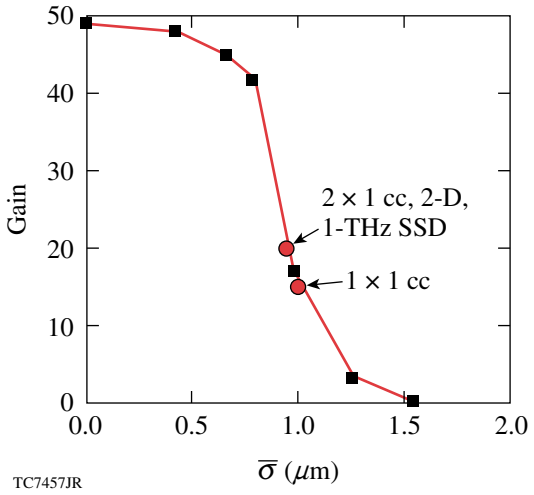

Figure 109.29
The dependence of gain on the parameter $\overline{\sigma}$ is shown, determined from simulations of initial ice-layer roughness for an ice spectrum with a power-law index of $\beta = 2$.

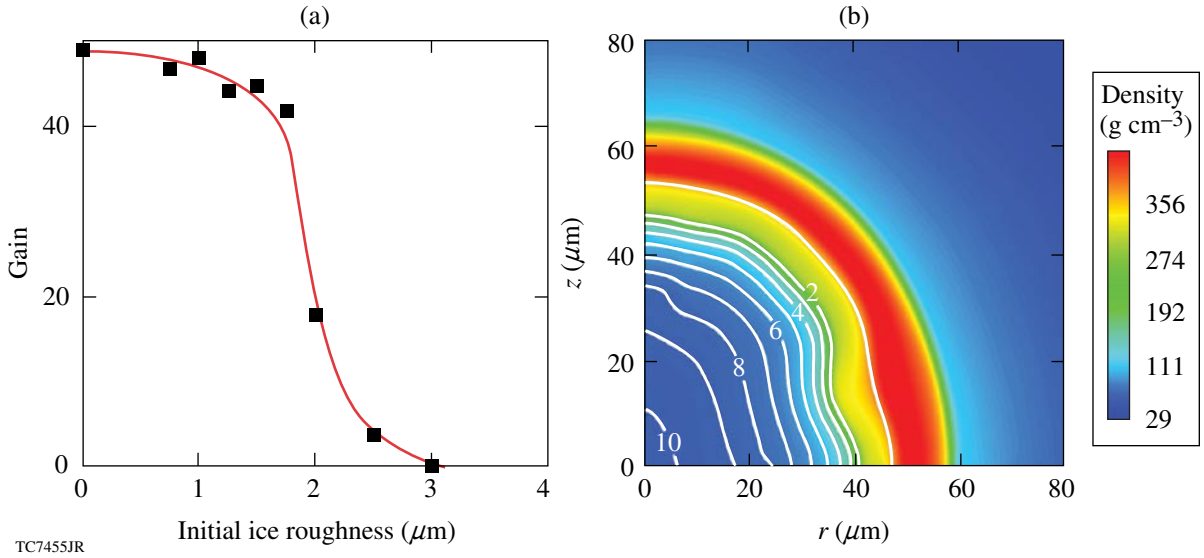

Figure 109.28
(a) The gain as a function of initial ice roughness for a power-law index of 2. This target tolerates an rms ice roughness of ~1.75 μm before deviation from the 1-D gain. (b) The shell at the time of ignition for the case of 1.75-μm-rms ice roughness is also shown. The gray scale shows mass density, and contour lines indicate ion temperature in keV. Note that the hot spot is primarily distorted by modes 2 to 6.

growth delays the onset of ignition, which consumes part of the margin leading to a lower burnup fraction at ignition.[22] The lower tolerance of this design compared to the 1.5-MJ design is due to the reduction in margin caused by the lowering of the incident laser-driver energy.

2. Outer-Surface Roughness

Foam-target fabrication at General Atomics has made significant strides in the past few years. Resorcinol-formaldehyde foam shells with submicron pore sizes (less than 0.25 μm) and thin (~5-μm) CH overcoats have been diagnosed using atomic-force microscopy.[30] The measured mode-amplitude spectrum shows spectral dependence roughly proportional to ℓ^{-2}, with most of the power in modes less than ten. The overall rms roughness for these foam shells has been shown to be as low as ~450 nm, about four times larger than that of the NIF's CH-surface standard roughness (Ref. 17 and references therein).

A 2-D simulation incorporating this surface spectrum, modeled as ribbon modes, resulted in a $\overline{\sigma}$ value of 0.38 μm and demonstrated negligible reduction in target gain. By comparison, a simulation using the NIF standard with an rms of ~115 nm produced a $\overline{\sigma}$ of 0.08 μm.

3. Multiple-Beam Nonuniformity

Multiple-beam nonuniformity, often referred to as beam-to-beam power imbalance, is caused by at least five sources of drive nonuniformity: variations in the power between the different laser beams, drive asymmetry caused by the geometry of the beam port locations and beam overlap, beam-pointing errors, and variations in beam timing. The nonuniformity spectrum has been determined as a function of time for the first four of these contributions for the wetted-foam laser pulse by spherical-harmonic decomposition of the illumination pattern of the beams projected onto the surface of the target. A harmonic modal spectrum is produced by combining all m modes in quadrature for each mode number ℓ. The symmetric NIF direct-drive port geometry contributes a constant perturbation, primarily in mode $\ell \le 6$. Beam mistiming, which is expected to have an rms value of 30 ps on the NIF,[26] produces perturbations in modes ℓ = 1 to 3, primarily during the rise and fall of the picket. Despite these perturbations, the mistiming of the picket was found to have a small effect on target performance.[31] The imbalance in energy between beams is expected to be ~8% rms on the NIF. The resulting perturbations are dominated by modes 2 to 12, with an amplitude of ~1%. The 2-D simulations described here include the effects of power imbalance between beams, beam overlap, and port geometry.

A series of six 2-D power-balance runs were performed. These simulations included modes 2 to 12, with 44 zones per wavelength of mode 12. They were performed using power-balance histories[17] adapted to the wetted-foam-design laser pulse. They produced an average reduction in gain of ~6%, with a $\overline{\sigma}$ of about 0.11 μm.

4. Single-Beam Nonuniformity

Single-beam nonuniformity or imprint is the source of nonuniformity capable of causing the greatest reduction in target yield, depending on the level of beam smoothing used. Illumination perturbations contribute to imprint through the perturbation in the laser-drive shock front and the acceleration perturbation in the post-shock region, which causes lateral flow in the shock-compressed material.[32] These produce secular growth during the foot pulse that seeds RT growth during the drive pulse. Several methods have been developed for reducing imprint. On the NIF these include SSD, distributed phase plates, and polarization smoothing. In the 2-D imprint simulations, we have modeled the effects of all three smoothing techniques. The DPP spectrum is modeled using an analytical fit for the laser speckle,[33] with amplitudes reduced to account for the effects of polarization smoothing and 40-beam overlap for the NIF's 192-beam system.

Two-dimensional SSD is modeled using a nondeterministic algorithm where the phase of each mode is assigned randomly every modal coherence time. The coherence time is given by a 2-D generalization of the formula $t_c = \left[\Delta\nu \sin\left(n_c \pi \ell / \ell_{\max}\right)\right]^{-1}$ (Ref. 34), where $\ell_{\max} = 2\pi R_0 / \delta$ is the mode number corresponding to half the speckle size δ, $\Delta\nu$ is the SSD bandwidth, and n_c is the number of color cycles on the laser system. The randomly chosen phases for each mode repeat after a number of coherence times, which depends on the mode number and the angular divergence in each dimension, implementing the asymptotic level of smoothing achievable by SSD. This asymptotic limit is much larger for 1-D SSD than for 2-D, resulting in much greater imprint, as will be seen below. For long-wavelength modes the number of statistically independent speckle patterns is small enough that a single simulation does not fully sample the ensemble of possible phase choices. For this reason, many of the runs here were repeated several times.

The reduction in growth rate due to ablative stabilization means the ablation-front mode spectrum due to imprint decreases with increasing mode number (see, e.g., Fig. 4 of Ref. 32). When this spectrum feeds through to the inner surface of the ice, there is an additional reduction in amplitude for increasing mode number due to the attenuation factor

exp(–$k\Delta R$). The ice spectrum at the end of the acceleration phase is shown in Fig. 109.30 for a simulation modeling the effects of imprint from modes ℓ = 2 to 200. Due to the initial mode-number dependence in the imprint spectrum and the feedthrough attenuation, modes above ℓ = 100 contribute less than 1% to the overall rms. For this reason, additional 2-D imprint runs were performed including only modes up to 100. To reduce the simulation time, only even modes are modeled in these simulations, with the amplitudes of the odd modes added in quadrature. These simulations use a resolution of 14 zones per wavelength at ℓ = 100, which has been found to be sufficient to resolve the smallest perturbation wavelengths.

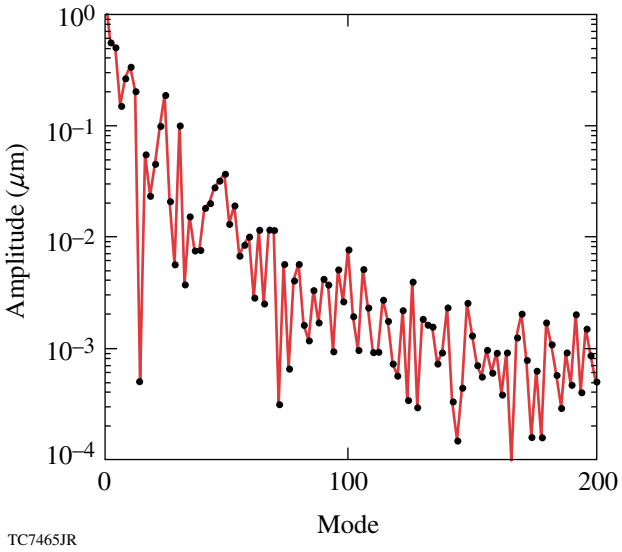

Figure 109.30
The DT-ice-roughness spectrum on the inner surface of the shell at the end of the acceleration phase for a simulation modeling the effects of imprint in modes up to ℓ = 200. Due to the mode-number dependence on the imprint spectrum and feedthrough attenuation, modes above ℓ ~ 100 contribute negligibly to the total rms.

The characteristic smoothing time T for SSD, given by the inverse of the smoothing rate, is related to the key SSD parameters by $T \sim (\nu_m n_c \delta)^{-1} \sim (\Delta\nu n_c)^{-1}$, where ν_m is the modulator depth. To determine the dependence of target performance on smoothing time, we have performed simulations for four different levels of SSD bandwidth: 1.33 THz, 0.89 THz (referred to here and elsewhere as "1-THz" SSD), 590 GHz, and 295 GHz. These all use one color cycle in each direction and modulator frequencies of 15.4 GHz and 2.81 GHz. The shell at the end of the acceleration phase is shown for each of these simulations in Fig. 109.31. The dependence of imprint on the bandwidth is clearly seen in the level of perturbation on the outer shell surface: whereas the shell from the 1.3-THz simulation is intact and relatively unperturbed, that from the ~0.3-THz simulation is completely broken up. The $\overline{\sigma}$ values for imprint alone are shown in Fig. 109.31: 0.37 μm, 0.86 μm, 0.96 μm, and 2.3 μm for 1.3 THz, 0.9 THz, 0.6 THz, and 0.3 THz, respectively. For comparison, the $\overline{\sigma}$ value from a simulation with 2-D, 1-THz SSD with two color cycles in one direction and one in the other is just 0.43 μm, half of that found with one color cycle in each direction and the same bandwidth. When the $\overline{\sigma}$ values from the simulations shown in Fig. 109.31 are combined in quadrature with those due to energy imbalance, port geometry and beam overlap, foam surface roughness, and 1-μm initial ice roughness, they are increased to 0.74 μm, 1.07 μm, 1.15 μm, and 2.43 μm. The projected gain factors from these sums are 39, 12, 8, and 0.008, respectively.

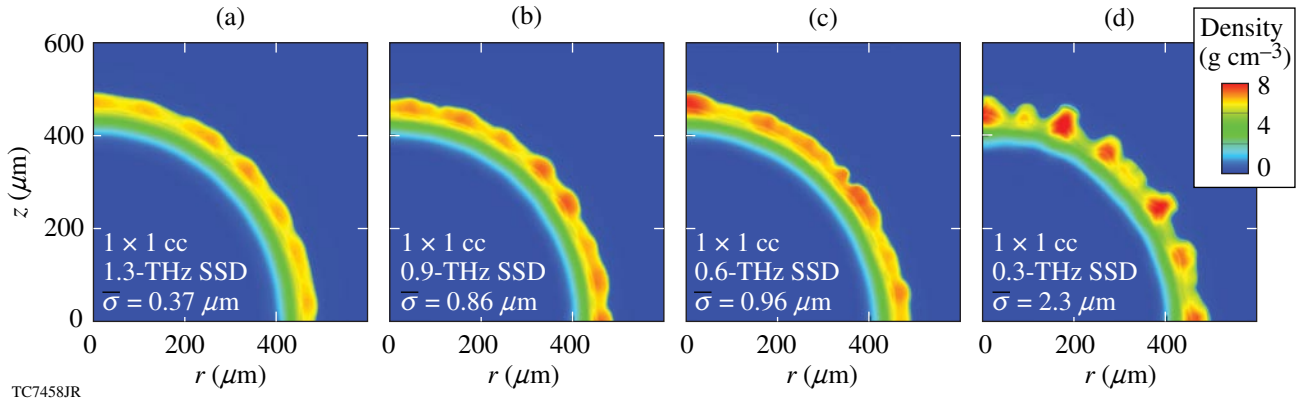

Figure 109.31
The shell is shown at the end of the acceleration phase for 2-D simulations of imprint modes 2 to 100, with one color cycle of SSD in each dimension and descending levels of bandwidth, showing the reduction in smoothing and the performance parameter $\overline{\sigma}$ just from imprint.

The SSD parameters that are currently anticipated for the NIF are much different from those required for an all-DT, direct-drive target at 1.5 MJ (Ref. 17), which we will refer to here as "2 × 1 SSD." The 2 × 1 SSD parameters are 2 and 1 color cycles in each direction, modulator frequencies of 15.4 GHz and 2.81 GHz, and a total UV bandwidth of 0.89 THz found by summing the individual bandwidths in quadrature. The anticipated NIF parameters for use with indirect-drive ignition (IDI) are 1-D SSD with 1.35 color cycles, a modulator frequency of 17 GHz, and a UV bandwidth of 185 GHz. These two sets of parameters have been simulated in 2-D, along with two intermediate levels of SSD: the 2 × 1 parameters but with just one color cycle in each direction ("1 × 1" SSD), and 2 × 1 SSD reduced to one dimension with two color cycles ("2 × 0" SSD). The shells at the end of the acceleration phase from multimode imprint simulations incorporating these levels of SSD are shown in Fig. 109.32. These simulations include all four sources of nonuniformity. The values of $\overline{\sigma}$ for these four simulations are 0.94 μm for the 2 × 1 SSD case, 1.0 μm for 1 × 1 SSD, 2.0 μm for 2 × 0 SSD, and 7.3 μm for IDI SSD. The projected gain factors for these integrated simulations are 21, 16, 0, and 0, respectively.

Integrated Simulations

Three integrated simulations were performed. The first two include drive asymmetry due to power imbalance and port geometry, surface roughness (370 nm), 0.75-μm initial ice roughness with a power-law index of $\beta = 2$, and single-beam imprint. The third uses a different initial ice spectrum with 2-D, 2 × 1 SSD beam smoothing and is discussed below.

The smoothing modeled in the first two simulations was polarization smoothing and either 2-D, 2 × 1 or 1-D, 2 × 0 SSD. The targets from these simulations, at the end of the acceleration phase and near the time of peak compression, are shown in Fig. 109.33. The 2-D SSD case has a much less perturbed shell at the end of acceleration than the 1-D SSD simulation. As a result, its hot spot is much more uniform at peak compression, showing primarily distortions with modes less than or equal to 6. The hot spot at this time (9.4 ns) is approximately 40 μm in size, and the neutron-averaged areal density is 1.31 g/cm^3. By comparison, the 1-D SSD simulation shows large perturbations at the end of acceleration that produce distortions over a wide spectral range at peak compression (9.3 ns). These distortions in the shell produce a more-distorted inner shell surface and lower ion temperatures at stagnation than in the 2-D SSD case and prevent the target from achieving gain greater than 1.

Smoothing levels due to 2-D and 1-D SSD are very different, even for long-wavelength modes. The shortest mode that can be smoothed by SSD is given by $\ell_{\min} = 2\pi R_0 / (2F\Delta\theta) \sim 4$ (Ref. 35), where F is the focal distance (7.7 m for the NIF) and $\Delta\theta^2 = \Delta\theta_1^2 + \Delta\theta_2^2$ is the effective far-field divergence, approximated by summing the contributions from each direction in quadrature. For 2 × 1, 2-D SSD, smoothing is effective above mode 4, and above mode 6 for 2 × 0, 1-D SSD. This is demonstrated in Fig. 109.34(a), which shows the smoothing due to SSD at 1 ns for modes up to 50. Note that even though the difference between 1-D and 2-D smoothing is small for modes less than 10, these modes also see less thermal smoothing[29] and a greater decoupling time than shorter-wavelength modes. Both 1-D and 2-D SSD smooth at the same rate prior to asymptoting. The difference in smoothing between 1-D and 2-D SSD is due to the difference in the asymptotic level. This is shown for mode number 22 in Fig. 109.34(b). For this

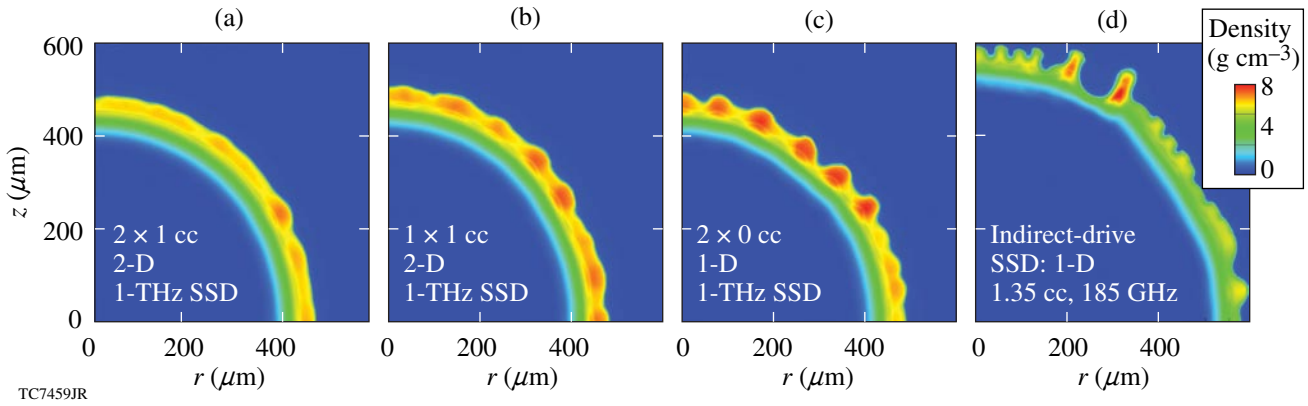

Figure 109.32
The shell at the end of the acceleration phase is shown for four 2-D simulations incorporating different sets of SSD parameters. These are integrated simulations that also include the effects of energy imbalance, foam-surface nonuniformity, and 1 μm of ice roughness.

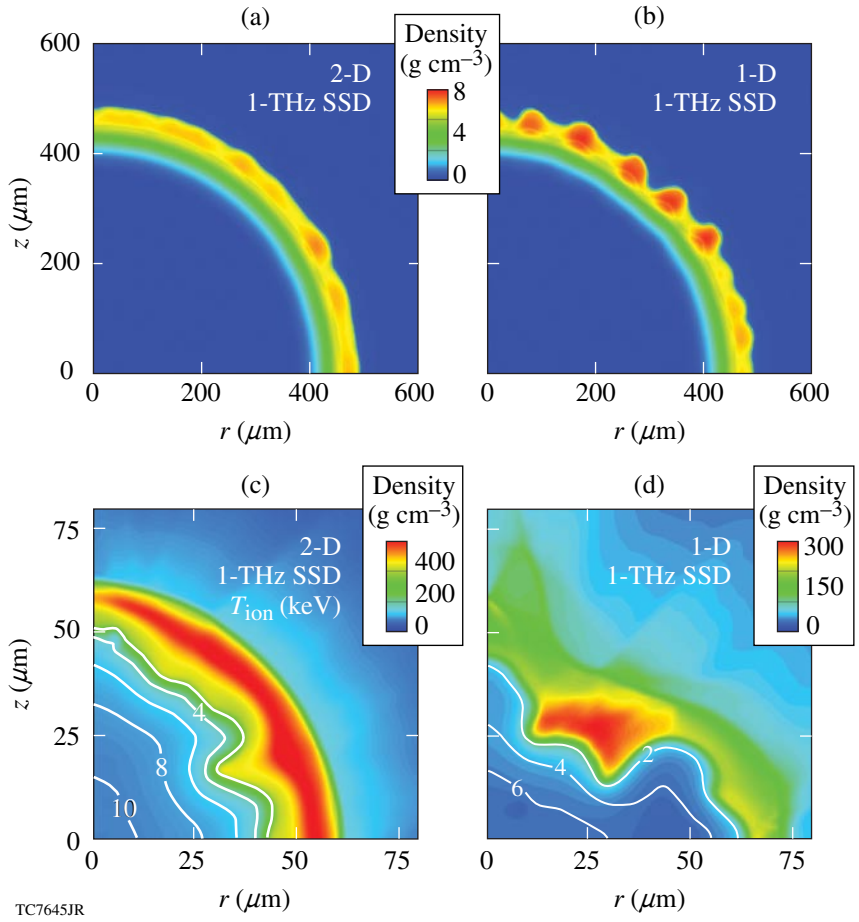

Figure 109.33
The shell is shown at the end of the acceleration phase [(a) and (b)] and near the time of peak compression [(c) and (d)] for the 2×1 and 2×0 SSD configurations, including all sources of nonuniformity. Unlike the integrated simulations shown in Fig. 109.32, these were run to completion. The high level of nonuniformity at the end of the acceleration phase and the highly distorted hot spot in the 2×0 case demonstrate the importance of 2-D SSD smoothing for target performance. The 2×1 simulation achieved a gain of 20, compared to a gain of less than 1 for the 2×0 case.

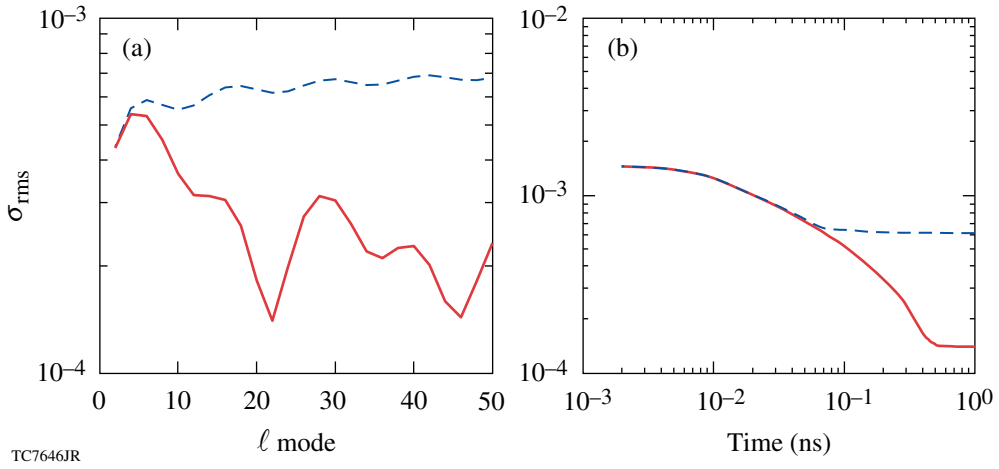

Figure 109.34
The smoothing due to SSD is shown in terms of (a) the mode number at 1 ns and (b) the perturbation for mode $\ell = 22$ as a function of time. Solid lines are 2-D SSD and dashed lines are 1-D SSD. These demonstrate the difference in the asymptotic level of smoothing for 1-D and 2-D SSD, as well as the level of smoothing for low mode numbers.

mode, the asymptotic level is reached at 70 ps for 1-D SSD and at 0.5 ns for 2-D SSD.

The third completed integrated simulation had the same nonuniformity levels and beam smoothing as the 2×1 just discussed, with an initial ice roughness of 1 μm and an ice power-law spectral index of $\beta = 1$. This was chosen to approximate the spectra of cryogenic DT capsules produced at LLE, which have less power in the low modes because of the different layering process. While the ice roughness was higher for this simulation than for the integrated 2-D SSD simulation described above, the lower power-law index reduces the spectral power in the low modes relative to the high modes. The combined effect is to produce a hot spot at peak compression, shown in Fig. 109.35, which is similar to that of the 2×1 SSD integrated simulation shown in Fig. 109.33(c), although with a smaller and more distorted hot spot. The gain factor of this simulation was 27. This shows that, for a smaller power-law index, the target can tolerate a greater ice roughness with little reduction in gain.

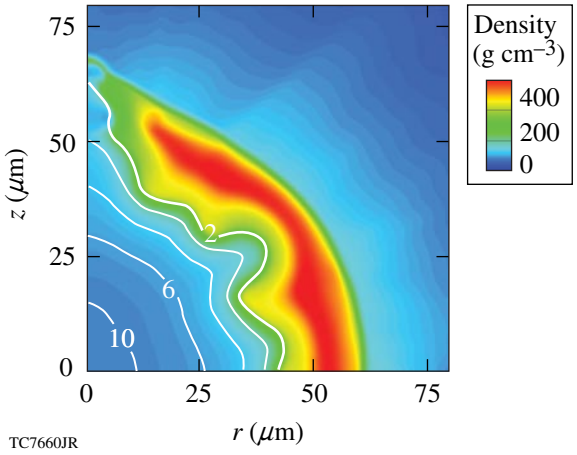

Figure 109.35
The shell is shown at peak compression for a simulation using 2-D, 2×1, 1-THz SSD with 1-μm initial ice roughness and an ice spectral index of 1. The resulting 2-D gain is 27.

Conclusions

An ignition target design using a wetted-foam ablator to couple greater laser energy into the target has been presented for use on the NIF with 1 MJ of incident laser energy. This design makes use of a thicker shell and lower implosion velocity to reduce the effects of imprint. A nonuniformity-budget analysis indicates that imprint, with 2-D, 2×1 color-cycle, 1-THz SSD smoothing, produces an effective nonuniformity $\overline{\sigma}$ that is slightly larger than that of the other sources of nonuniformity, namely, power imbalance, outer-surface roughness, and ice roughness. With 1×1 SSD the effective nonuniformity is more than twice that from other sources.

Simulations suggest that this design will ignite and achieve gain only if 2-D SSD is used to smooth single-beam illumination nonuniformities. The need for 2-D SSD has been found in other target-design performance studies as well.[17,36] Integrated simulations including imprint, surface and ice roughness, and beam-to-beam power imbalance were completed for two levels of SSD: 2×1 and 2×0, and 0.75-μm initial ice roughness with a power-law index of $\beta = 2$. The former achieved a gain of 32 compared to less than 1 for the latter. The difference in performance is due primarily to the difference in the asymptotic level of smoothing for 2-D and 1-D SSD. A third integrated simulation was completed using 1-μm initial ice roughness with a power-law index of $\beta = 1$, meant to approximate the ice spectra found in DT cryogenic targets at LLE. This simulation also ignited, achieving a gain factor of 27. This indicates that greater ice nonuniformity may be tolerated if combined with a smaller spectral index.

ACKNOWLEDGMENT

This work was supported by the U.S. Department of Energy Office of Inertial Confinement Fusion under Cooperative Agreement No. DE-FC52-92SF19460, the University of Rochester, and the New York State Energy Research and Development Authority. The support of DOE does not constitute an endorsement by DOE of the views expressed in this article.

REFERENCES

1. J. Paisner *et al.*, Laser Focus World **30**, 75 (1994).
2. J. Nuckolls *et al.*, Nature **239**, 139 (1972).
3. J. D. Lindl, Phys. Plasmas **2**, 3933 (1995).
4. S. Atzeni and J. Meyer-ter-Vehn, *The Physics of Inertial Fusion: Beam Plasma Interaction, Hydrodynamics, Hot Dense Matter*, International Series of Monographs on Physics (Clarendon Press, Oxford, 2004).
5. A. J. Martin, R. J. Simms, and R. B. Jacobs, J. Vac. Sci. Technol. A **6**, 1885 (1988); J. K. Hoffer and L. R. Foreman, Phys. Rev. Lett. **60**, 1310 (1988).
6. S. Skupsky, R. W. Short, T. Kessler, R. S. Craxton, S. Letzring, and J. M. Soures, J. Appl. Phys. **66**, 3456 (1989).
7. T. R. Boehly, V. A. Smalyuk, D. D. Meyerhofer, J. P. Knauer, D. K. Bradley, C. P. Verdon, and D. Kalantar, in *Laser Interaction and Related Plasma Phenomena*, edited by G. H. Miley and E. M. Campbell (American Institute of Physics, New York, 1997), Vol. 406, pp. 122–129.
8. Y. Lin, T. J. Kessler, and G. N. Lawrence, Opt. Lett. **20**, 764 (1995).

9. T. W. Johnston and J. M. Dawson, Phys. Fluids **16**, 722 (1973).

10. L. M. Hair *et al*., J. Vac. Sci. Technol. A **6**, 2559 (1988); R. A. Sacks and D. H. Darling, Nucl. Fusion **27**, 447 (1987).

11. D. G. Colombant *et al*., Phys. Plasmas **7**, 2046 (2000).

12. M. Tabak, *ICF Program Annual Report 1989 (U)*, Lawrence Livermore National Laboratory, Livermore, CA, UCRL-LR-116901-88/80, 141 (1989).

13. S. Skupsky, R. Betti, T. J. B. Collins, V. N. Goncharov, D. R. Harding, R. L. McCrory, P. W. McKenty, D. D. Meyerhofer, and R. P. J. Town, in *Inertial Fusion Sciences and Applications 2001*, edited by K. Tanaka, D. D. Meyerhofer, and J. Meyer-ter-Vehn (Elsevier, Paris, 2002), pp. 240–245.

14. J. D. Sethian *et al*., Nucl. Fusion **43**, 1693 (2003).

15. M. Desselberger *et al*., Phys. Rev. Lett. **74**, 2961 (1995).

16. P. B. Radha, V. N. Goncharov, T. J. B. Collins, J. A. Delettrez, Y. Elbaz, V. Yu. Glebov, R. L. Keck, D. E. Keller, J. P. Knauer, J. A. Marozas, F. J. Marshall, P. W. McKenty, D. D. Meyerhofer, S. P. Regan, T. C. Sangster, D. Shvarts, S. Skupsky, Y. Srebro, R. P. J. Town, and C. Stoeckl, Phys. Plasmas **12**, 032702 (2005).

17. P. W. McKenty, V. N. Goncharov, R. P. J. Town, S. Skupsky, R. Betti, and R. L. McCrory, Phys. Plasmas **8**, 2315 (2001).

18. G. Hazak *et al*., Phys. Plasmas **5**, 4357 (1998).

19. T. J. B. Collins, A. Poludnenko, A. Cunningham, and A. Frank, Phys. Plasmas **12**, 062705 (2005).

20. R. Betti, K. Anderson, T. R. Boehly, T. J. B. Collins, R. S. Craxton, J. A. Delettrez, D. H. Edgell, R. Epstein, V. Yu. Glebov, V. N. Goncharov, D. R. Harding, R. L. Keck, J. H. Kelly, J. P. Knauer, S. J. Loucks, J. A. Marozas, F. J. Marshall, A. V. Maximov, D. N. Maywar, R. L. McCrory, P. W. McKenty, D. D. Meyerhofer, J. Myatt, P. B. Radha, S. P. Regan, C. Ren, T. C. Sangster, W. Seka, S. Skupsky, A. A. Solodov, V. A. Smalyuk, J. M. Soures, C. Stoeck, W. Theobald, B. Yaakobi, C. Zhou, J. D. Zuegel, J. A. Frenje, C. K. Li, R. D. Petrasso, and F. H. Séguin, Plasma Phys. Control. Fusion **48**, B153 (2006).

21. V. N. Goncharov, P. McKenty, S. Skupsky, R. Betti, R. L. McCrory, and C. Cherfils-Clérouin, Phys. Plasmas **7**, 5118 (2000).

22. W. K. Levedahl and J. D. Lindl, Nucl. Fusion **37**, 165 (1997).

23. V. N. Goncharov, J. P. Knauer, P. W. McKenty, P. B. Radha, T. C. Sangster, S. Skupsky, R. Betti, R. L. McCrory, and D. D. Meyerhofer, Phys. Plasmas **10**, 1906 (2003); K. Anderson and R. Betti, Phys. Plasmas **10**, 4448 (2003).

24. K. Anderson and R. Betti, Phys. Plasmas **11**, 5 (2004); R. Betti, K. Anderson, J. Knauer, T. J. B. Collins, R. L. McCrory, P. W. McKenty, and S. Skupsky, Phys. Plasmas **12**, 042703 (2005).

25. T. J. B. Collins and S. Skupsky, Phys. Plasmas **9**, 275 (2002).

26. O. S. Jones *et al*., in *NIF Laser System Performance Ratings*, Supplement to Third Annual International Conference on Solid State Lasers for Application to Inertial Confinement Fusion (SPIE, Bellingham, WA, 1998), Vol. 3492, pp. 49–54.

27. V. N. Goncharov, S. Skupsky, P. W. McKenty, J. A. Delettrez, R. P. J. Town, and C. Cherfils-Clérouin, in *Inertial Fusion Sciences and Applications 99*, edited by C. Labaune, W. J. Hogan, and K. A. Tanaka (Elsevier, Paris, 2000), pp. 214–219.

28. R. Kishony and D. Shvarts, Phys. Plasmas **8**, 4925 (2001).

29. S. E. Bodner, J. Fusion Energy **1**, 221 (1981).

30. J. Hund and A. Nikroo, General Atomics, private communication (2006).

31. R. Epstein, T. J. B. Collins, J. A. Delettrez, V. N. Goncharov, J. P. Knauer, J. A. Marozas, P. W. McKenty, P. B. Radha, and V. A. Smalyuk, Bull. Am. Phys. Soc. **50**, 114 (2005).

32. V. N. Goncharov, S. Skupsky, T. R. Boehly, J. P. Knauer, P. McKenty, V. A. Smalyuk, R. P. J. Town, O. V. Gotchev, R. Betti, and D. D. Meyerhofer, Phys. Plasmas **7**, 2062 (2000).

33. R. Epstein, J. Appl. Phys. **82**, 2123 (1997).

34. J. E. Rothenberg, J. Opt. Soc. Am. B **14**, 1664 (1997).

35. S. Skupsky and R. S. Craxton, Phys. Plasmas **6**, 2157 (1999).

36. S. V. Weber, S. G. Glendinning, D. H. Kalantar, M. H. Key, B. A. Remington, J. E. Rothenberg, E. Wolfrum, C. P. Verdon, and J. P. Knauer, Phys. Plasmas **4**, 1978 (1997).